Pergamon

Int. J. Heat Mass Transfer. Vol. 40, No. 14, pp. 3305–3321, 1997

Printed in Great Britain
0017–9310/97 $17.00+0.00

PII: S0017–9310(96)00380–8

Local convective heat transfer to submerged pulsating jets

E. C. MLADIN† and D. A. ZUMBRUNNEN‡

Department of Mechanical Engineering, Laboratory for Materials Processing and Industrial Mixing, Clemson University, Clemson, SC 29634-0921, U.S.A.

(*Received* 14 *June* 1996 *and in final form* 5 *November* 1996)

Abstract—An experimental investigation was performed to study the effect of flow pulsations on the local heat transfer characteristics of a planar air jet. A microsensor provided localized and essentially instantaneous heat flux and temperature signals. Heat transfer and thermal anemometry flow measurements were synchronized to associate influences of periodic flow structures and pulsations on heat transfer. Pulsation frequencies corresponded to Strouhal numbers below 0.106, and pulse amplitude was varied from 0 to 50% of the mean flow velocity. Nusselt numbers in the nozzle mid-plane increased by up to 12%, and by up to 80% at distances downstream. © 1997 Elsevier Science Ltd.

1. INTRODUCTION

The heat transfer characteristics of an impinging jet, whether circular or planar, can often be correlated with the characteristics of the corresponding non-impinging jet [1, 2]. It is therefore interesting to note that large coherent flow structures can evolve within shear layers formed between a free jet flow and a surrounding still fluid. In pulsed flows, for both planar and circular submerged jets, the size and formation of coherent structures are influenced by the pulse amplitude and pulse frequency [3, 4]. Rockwell and Niccolls [5] used high-speed photographs to reveal the formation and natural breakdown of flow structures in an unforced planar jet. Vortices formed either symmetrically or alternately about the nozzle centerline, and decayed after merging to yield larger vortices. Farrington and Claunch [6] used infrared imaging and smoke-wire visualization to determine the influence of flow pulsations on these flow structures. Their results for jets with $Re_w = 7200$ and $0 < St_w < 0.324$ are the basis for Fig. 1. In the pulsating jets ($St_{w,1}$ and $St_{w,2}$), vortex formation occurred closer to the nozzle, and vortices were larger than in the steady-jet case ($St_w = 0$). As a result, entrainment increased, and the length of the potential core was shortened. An irregular vortex pattern was transformed by the pulsations to a more organized and periodic vortex train that was symmetric with the nozzle axis. Larger vortices led to a wider spread angle for the potential core and accelerated entrainment.

Kataoka *et al.* [7] documented that stagnation-point heat transfer in axisymmetric submerged jets is enhanced by a surface renewal effect produced by the impingement of large-scale structures on the boundary layer. The maximum Nusselt number at the stagnation point corresponded to flow conditions where surface renewal had the maximum frequency. Donaldson *et al.* [2] investigated the turbulence structure of steady, nonimpinging and impinging circular air jets. For nozzle-to-plate separation distances greater than about 10 nozzle diameters, turbulence intensities

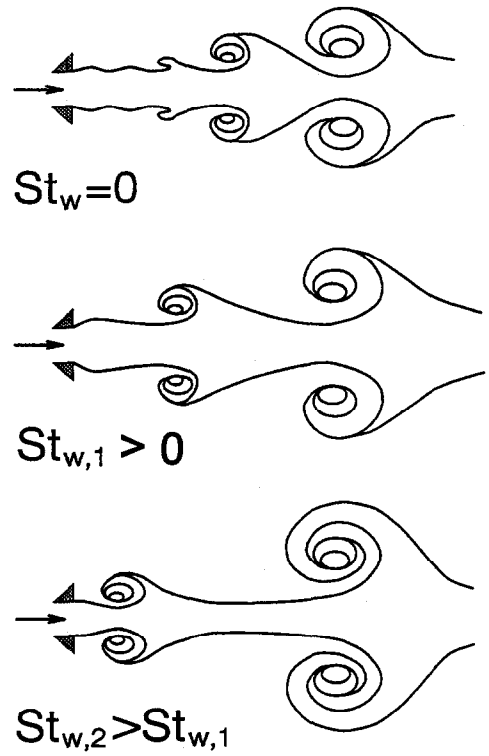

Fig. 1. Effect of pulsations on the development of a non-impinging jet [6].

†Current address: Polytechnic University, Mechanical Engineering Department, Bucharest, Romania.

‡Author to whom correspondence should be addressed.

NOMENCLATURE

A_N	flow pulse amplitude $\tilde{V}_{rms}/\bar{V}$
C	free stream velocity gradient for nonpulsating jet
C_*	dimensionless free stream velocity gradient, Cw/V
f_{ex}	excitation/forcing frequency in pulsed jet flows
f_*	dimensionless pulsation frequency, f_{ex}/C
h	convective heat transfer coefficient
H	nozzle-to-plate separation distance
k	thermal conductivity of fluid
Nu_w	Nusselt number, hw/k_f
q_s	convective heat flux
Pr	Prandtl number
Re_w	Reynolds number, $w\bar{V}_N/\nu_f$
St_w	Strouhal number, $wf_{ex}/\bar{V}_N$
t	time
T_j	jet temperature
T_s	surface temperature
Tu	turbulence intensity, equation (7)
Tu_{fl}	overall disturbance level, equation (6)
U_∞	local free stream velocity component parallel to the surface
V	jet flow velocity
V'	fluctuating velocity component due to turbulence, equation (1)
w	nozzle width or diameter
x	distance along impingement surface from stagnation line
y_N	downstream distance along nozzle axis from the nozzle exit.

Greek symbols

Γ	dimensionless thermal boundary layer thickness, $C\Delta^2/\nu_f$
δ	hydrodynamic boundary layer thickness
Δ	thermal boundary layer thickness
ε_1	ratio of peak velocity to mean velocity for a sinusoidal pulsation in incident flow velocity
ν	kinematic viscosity.

Subscripts

avg	time-averaged value
f	pertaining to film temperature T_f, $(T_s+T_\infty)/2$
N	pertaining to nozzle exit
S	pertaining to stagnation line ($x = 0$).

Superscripts

$\bar{}$	time-averaged (arithmetic mean)
$\tilde{}$	periodic component with zero mean.

and mean velocities differed from those of a free jet only within a distance of less than about two nozzle diameters from the plate. Marked increases in turbulence intensities were measured in the free stream close to the surface. Popiel and Trass [4] investigated flow structures of unforced free and impinging circular jets with a smoke-wire flow visualization technique. Photographs indicated that the presence of an impingement plate does not affect upstream vortical structures. Large-scale toroidal vortices which were incident on the plate induced consecutive ring-shaped wall eddies. Favre-Marinet and Binder [8] studied experimentally the influence of large amplitude flow pulses on the development of a circular, nonimpinging air jet. Consistent with Farrington and Claunch [6], their results indicated that jets with large amplitude pulsations in the jet flow entrained surrounding fluid more rapidly, and thereby decayed more quickly than steady jets. Periodic fluctuations were amplified over a distance of two to three nozzle diameters, but were essentially abated at a distance of 10 diameters from the nozzle opening. The pulse decay was accompanied by a large increase in turbulence intensity as energy was transferred from periodic flow structures to turbulent motion. It seems reasonable to assume that mixing within the boundary layer is related closely to the formation and interaction of flow structures in the corresponding nonimpinging jet. Any mechanism which alters this process may lead to changed and, perhaps, enhanced heat transfer conditions. Thus, an opportunity to enhance heat transfer by pulsating a jet flow is suggested by these results. Such enhancement mechanisms are particularly important to materials processing and manufacturing applications of impinging jets, since the surfaces of manufactured goods often cannot be modified to improve heating, cooling or drying conditions.

Heat transfer to pulsating jets has been investigated in a few prior studies. Nevins and Ball [9] measured spatially and temporally averaged heat transfer from a flat isothermal surface cooled by a pulsating circular air jet with $1200 < Re_w < 12000$ and low Strouhal numbers ($10^{-4} < St_w < 10^{-2}$). Nozzle-to-plate separation distances from eight to 32 nozzle diameters were considered. Nusselt numbers were independent of pulse amplitude, frequency and waveform. Changes to heat transfer were not evident, perhaps since measurements were restricted to very low Strouhal numbers, where steady flow characteristics may have prevailed. More recently, high-frequency ($St_w > 0.26$) pulsations in on/off (i.e. intermittent) unsubmerged planar water jets led to increases in local Nusselt numbers of up to about 100% for $3100 < Re_w < 21000$ [10]. Nonlinear dynamics models of momentum and

energy transport in the boundary layers [11, 12] were used to estimate pulsation frequencies above which repeated boundary layer development events in an intermittent jet flow can lead to enhancement. Predictions were in very good agreement with experimental results. Sheriff and Zumbrunnen [13] measured local, time-averaged heat transfer coefficients along a constant heat flux surface cooled by a pulsating unsubmerged planar water jet where the flow velocity varied sinusoidally for $3150 < Re_w < 15\,800$ and $0.012 < St_w < 0.144$. Their results indicated no measurable change in the Nusselt number for pulse amplitudes below 40% of the average flow velocity. However, reductions in Nusselt numbers became measurable at higher pulse amplitudes. At a pulse amplitude of 85%, the stagnation line Nusselt number decreased by 17%, with reductions decreasing monotonically away from the stagnation line. The reductions were due chiefly to nonlinear dynamic responses of momentum and energy transport within the boundary layers to the flow pulsations [14]. Similar reductions were reported for pulsating air jets issuing from long tubes [15], where highly organized flow structures such as those in Fig. 1 would not be expected to occur [16].

In light of changes observed in the flow structures of submerged jets due to flow pulsations as depicted in Fig. 1, and complex responses predicted in the boundary layer dynamics [12, 14], it was deemed appropriate to investigate whether heat transfer enhancement can be obtained by inducing flow pulsations in an incident submerged-jet velocity. Planar, pulsating air jets were used, and a surface-mounted microsensor provided localized and essentially instantaneous heat flux and temperature signals. Heat transfer and thermal anemometry flow measurements were synchronized in order to associate influences of periodic flow structures and pulsations on heat transfer. Experiments were performed for steady and pulsating jets at jet Reynolds numbers of 1000, 5500 and 11 000. Pulsation frequencies ranged from 0 to 80 Hz, corresponding to Strouhal numbers below 0.106 based on nozzle width and jet discharge velocity. The pulse amplitude at the nozzle exit was varied from 0 to 50% of the mean flow velocity. The effects of Reynolds number, pulse frequency, and pulse amplitude on time-averaged and instantaneous heat transfer distributions were assessed.

2. EXPERIMENTAL APPARATUS AND PROCEDURES

A schematic of the experimental apparatus is shown in Fig. 2. Filtered and dehumidified air was directed to an air reservoir via a pressure regulator. Air flow to the nozzle was partitioned through a parallel flow network by one of two needle valves. In one branch of this network, air from the reservoir flowed with little restriction to the plenum box of the nozzle. In the other branch, the air flow was periodically interrupted by the continuous rotation of a ball valve. Rotation was provided by a variable-speed direct-current motor. A position indicator was constructed and installed on the motor shaft which consisted of a disk with two opposing narrow slots, a light-emitting diode, and a photoelectric sensor. The position of the ball valve and the phase within the pulse cycle were thereby detectable from a series of electrical spikes generated when light passed through either of the two slots. A specific pulse amplitude was obtained by adjusting with the needle valves the amount of flow through each branch of the network. The air reservoir and damping chambers promoted a nearly sinusoidal pulse waveform. A laminar flow element (LFE) was used to assess equipment performance, and was left isolated during experiments by shutting an upstream ball valve. Thermal anemometry equipment was calibrated in place with a separate pitot tube (not shown).

In order to produce a planar jet of low initial turbulence intensity and uniform spatial velocity profile across the nozzle width, a convergent geometry was used, and air flow was provided symmetrically to a plenum box with internal baffle plates and a honeycomb flow element. The nozzle had an inlet opening of 25×50 mm, and an outlet opening of 5×50 mm. A 70 mm convergent section was followed by a straight transition section 5 mm in length. A 120×100 mm extension plate was attached flush to the nozzle opening such that a flat, continuous surface extended parallel to the impingment surface. In this manner, the jet flows beyond the nozzle were not influenced by the specific size and external geometry of the nozzle body. This arrangement was also more representative of jets issued within jet arrays [17]. The plenum box was attached to a traversing mechanism in order to vary the separation distance between the nozzle opening and the impingement surface. The jets discharged upwards onto a 5 mm thick aluminum nitride ceramic plate that was 100 mm long and 50 mm wide. Discharging the jets upwards provided a thermally stable flow to obviate possible influences due to gravity. Heat was provided to the unexposed surface of the ceramic plate by passing electrical current through a thin nickel–chromium foil. The plate and foil were mounted on a phenolic box which also provided connection points between the foil, copper bus bars, and a direct-current power supply. Aluminum nitride is a high thermal conductivity material, so surface temperatures remained very nearly spatially and temporally constant as will be discussed.

Local heat flux and surface temperature signals were obtained with a microsensor manufactured by Vatell Corporation (Christiansburg, VA) for the specific purpose of this study. (Fabrication and operating procedures for similar microsensors are discussed by Hager *et al.* [18].) The microsensor, which is shown in Fig. 3, was fabricated directly onto the aluminum nitride impingement plate. The microsensor consisted of a thin-film heat flux gage and a resistance temperature sensor. The heat flux sensor (HFS) was for-

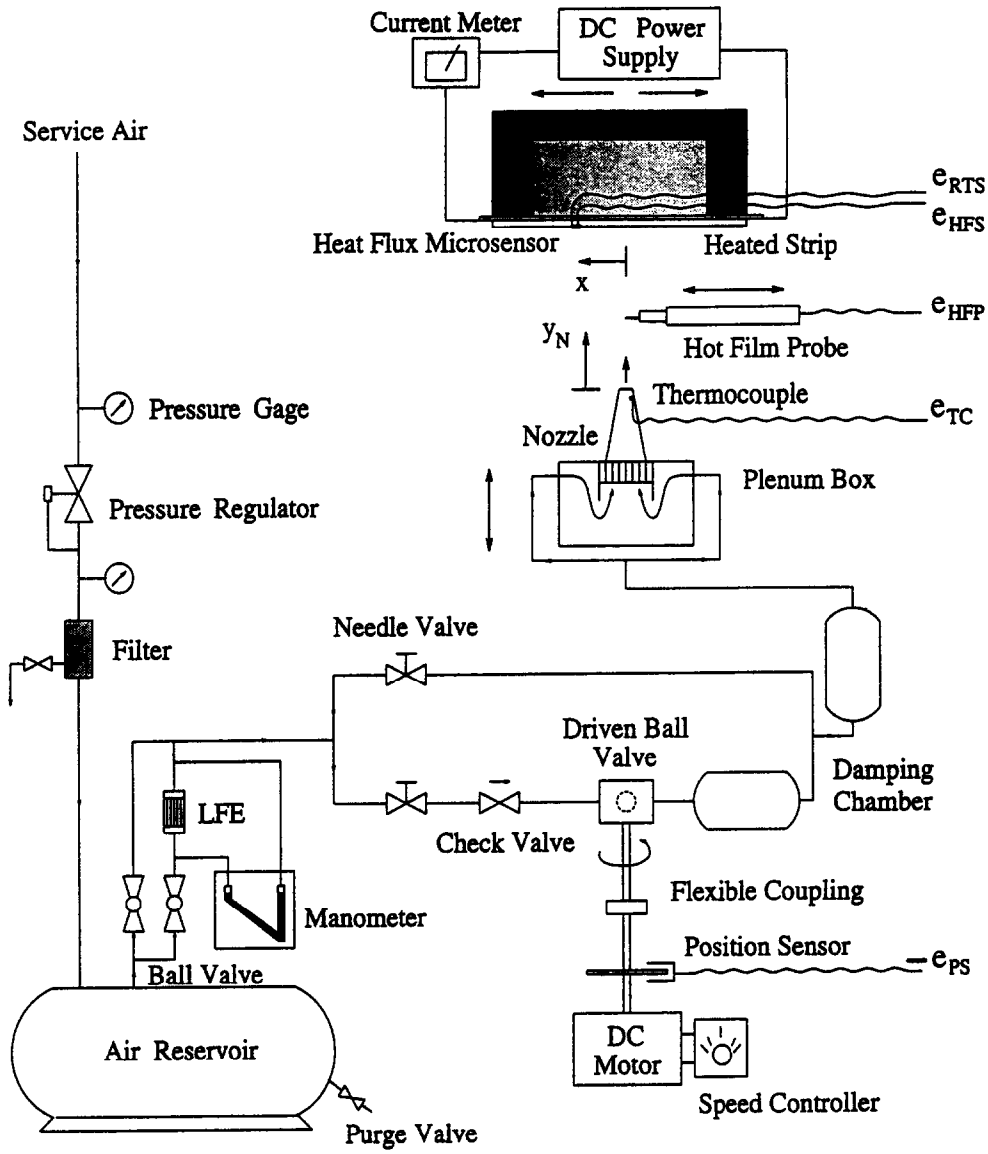

Fig. 2. Schematic representation of the experimental apparatus.

med of a thermal resistance layer with thermocouple temperature sensors on both sides [Fig. 3(a)]. The temperature sensing layers consisted of 250 nickel–nichrome thermocouple junctions placed in series to form a differential thermopile. The thermocouple layers were separated by a silicon monoxide thermal resistance layer of 1.4 μm thickness [Fig. 3(b)]. Corresponding surface temperature measurements were provided by a resistance temperature sensor (RTS) in the form of a platinum thin-film. Both the HFS and RTS were in a linear configuration [Fig. 3(c)], and were separated by about 0.2 mm. The sensors were oriented in the direction parallel to the length of the nozzle slot opening. The entire active portion of the microsensor occupied an area of 1.2×25 mm. Since the sensor length was half the spanwise dimension of the nozzle and plate, measurements were taken within portions of the planar jet where a two-dimensional flow field prevailed. The linear configuration and small size in comparison to the nozzle width yielded good localization of both heat flux and surface temperature measurements with good sensitivity. An overall thickness of less than 2 μm ensured that little thermal distortion occurred. Essentially instantaneous measurements were possible since the 20 μs sensor time response was very much smaller than both the pulse period and time intervals for turbulence fluctuations. Calibration information and related measurement uncertainties for the RTS were provided by the sensor manufacturer. The HFS was calibrated *in situ* with a transient heat conduction model of the substrate plate according to the approach described by Holmberg and Diller [19]. In this approach, microsensors that are deposited on thick surfaces are calibrated by minimizing differences between heat flux readings and calculated values from an analytical

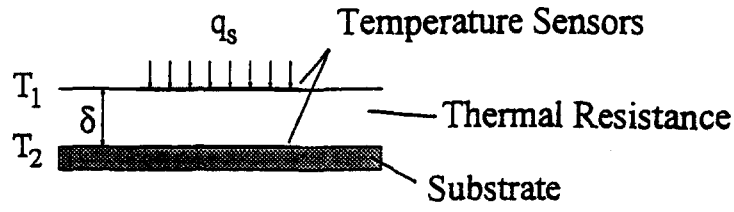

(a) Layered Heat Flux Gage

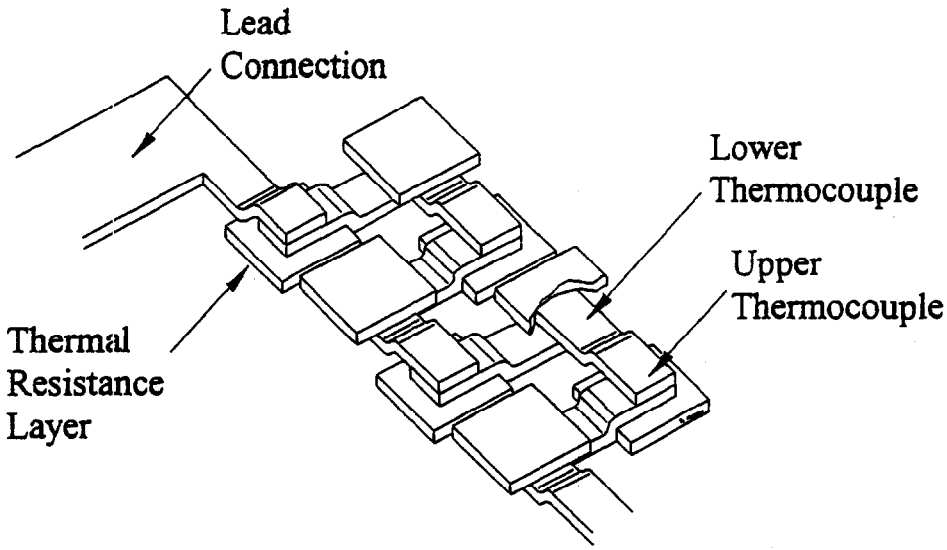

(b) Detailed Section of HFS

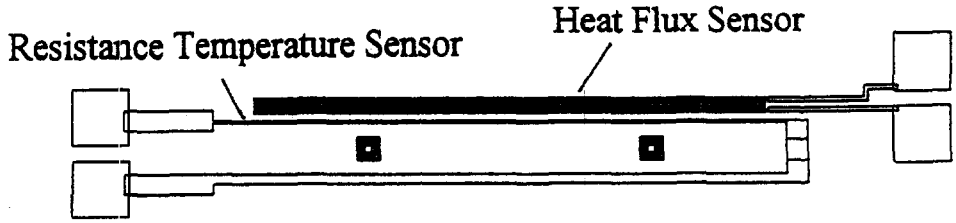

(c) Actual Layout of HFS and RTS

Fig. 3. Construction and layout of the heat flux microsensor.

transient heat conduction model of the substrate plate. Uncertainties in the heat flux calibration accounted for uncertainties in thermophysical properties of the substrate and were estimated by the sequential perturbation method [20] applied to the heat conduction model.

Heat transfer measurements at specific horizontal distances from the nozzle plane were performed by moving the phenolic box. The sensor was therefore fabricated on the ceramic impingement plate at an off-center location to allow measurements to be made at large horizontal distances from the nozzle. It is important to note that boundary layer development was unaffected by repositioning the sensor owing to the uniform design of the 5 mm thick aluminum nitride impingement plate and electrically heated foil. The measured surface heat flux ranged from 0.3 to 0.9 W cm^{-2}, and corresponded to surface temperatures between 50 and 96°C. Differences in jet and surface temperatures for any particular experiment differed spatially over a distance of 10 nozzle widths from the stagnation line by less than 6%. Temporal variations in temperature was less than 1%. Both variations were small due to the high thermal conductivity of alumi-

num nitride substrate plate. The heating condition of the experiments was therefore nearly that of a uniform and constant surface temperature.

Thermal anemometry operated in the constant temperature mode was used for the jet velocity measurements. The anemometer probe consisted of a single axis cylindrical hot-film sensor. A probe extension was mounted on a traversing mechanism with three degrees of freedom so that the sensor could be located to within 0.25 mm of a desired location in the flow field. The sensor was oriented horizontally in a cross-flow configuration. In this manner, accurate measurements could be obtained of the two-dimensional mean jet flow. The jet flow field was characterized in terms of time-averaged velocity, velocity pulse profile, and turbulence intensity within the nozzle plane of symmetry. Flow velocities fluctuated due to both turbulence and induced pulsations. The pulsating turbulent velocity field was represented by

$$V(t) = \bar{V} + \tilde{V}(t) + V'(t) \tag{1}$$

where $\bar{V}$ was the mean (time-averaged) component, $\tilde{V}$ represented the periodic component, and V' corresponded to the turbulent motion. Direct time-averaging of all instantaneous velocity measurements determined $\bar{V}$. In order to separate the turbulent component from the periodic one, measurements must be statistically averaged over many pulsation cycles. Common techniques which are used for this purpose are phase-averaging [21] and ensemble-averaging [22]. Both techniques assume that the instantaneous flow-field is represented by equation (1). The shaft position sensor (Fig. 2) did not give continuous information, but, instead, provided a sharp signal during each cycle. Since data were not available to account for phase synchronization, the ensemble-averaging technique was chosen for flow-field decomposition. For each set of flow parameters, many simultaneous velocity and shaft position measurements for hundreds of cycles were recorded. Signals from the shaft position sensor were used to synchronize each pulse to account for small cycle-to-cycle variations in the pulse period. For N cycles, the ensemble-average of data associated with the same time t_i from the beginning of each cycle was defined as

$$\langle V(t_i)\rangle = \lim_{N\to\infty} \frac{1}{N} \sum_{k=1}^{N} V_k(t_i) \tag{2}$$

where $V_k(t_i)$ was the ith velocity value in the kth sample cycle. This procedure was repeated for every time-point in the cycle ($1 < i < N$), resulting in the ensemble-averaged waveform $\langle V(t)\rangle$. In effect, the ensemble-averaging technique rejected the random background turbulence and extracted the organized (repeatable) motion from the total signal.

For homogeneous and isotropic fluctuations in stationary functions, the difference between an ensemble average and a time-average defines the cyclic or periodic velocity:

$$\tilde{V}(t) = \langle V(t)\rangle - \bar{V}. \tag{3}$$

The total fluctuating velocity V_{fl} consisted of a turbulent component and a periodic component, and was calculated by subtracting the mean velocity from the instantaneous velocity given by equation (1):

$$V_{\text{fl}}(t) = V(t) - \bar{V}. \tag{4}$$

The random turbulent velocity fluctuations were assumed to be statistically independent of the periodic velocity fluctuations. The flow unsteadiness was therefore characterized in terms of the overall disturbance level Tu_{fl}, the turbulence intensity level Tu, and the pulsation amplitude A. The relationships below were implemented after Evans [22]:

$$Tu_{\text{fl}}^2 = Tu^2 + A^2 \tag{5}$$

where

$$Tu_{\text{fl}} = \frac{1}{\bar{V}} \sqrt{\frac{1}{nN} \sum_{j=1}^{nN} V_{\text{fl}_j}^2} \tag{6}$$

$$Tu = \frac{1}{\bar{V}} \sqrt{\frac{1}{nN} \sum_{j=1}^{nN} V_j'^2} \tag{7}$$

$$A = \frac{1}{\bar{V}} \sqrt{\frac{1}{N} \sum_{j=1}^{N} \tilde{V}_j^2}. \tag{8}$$

The pulsation amplitude A in equation (5) should be distinguished from a peak-to-mean amplitude for a pure sinusoidal pulse waveform. Such a peak-to-mean amplitude is equal to $A\sqrt{2}$. The turbulence intensity Tu was computed for steady jets ($A = 0$, $Tu_{\text{fl}} = Tu$) from equation (7) with the turbulent velocity fluctuations obtained by subtracting the mean velocity component from the instantaneous velocity field. For pulsed-jet flows, the turbulence intensity level Tu was computed from equation (5) with values for Tu_{fl} and A. This approach [22] shortened the computation times required for data reduction associated with pulsed jets. Comparison for a few pulsed-jet cases of turbulence intensities computed with equations (5) and (7) indicated that the two equations yielded values with differences of less than 1%.

The selected sampling rates were based upon a compromise between hardware limitations, satisfactory performance for all sensors, and the desired physical mechanism to be captured. These countervailing requirements were met by setting the sampling rate at 4 kHz per channel or higher, such as to record about 100 readings for each pulse cycle and channel over about 600 cycles. Once the desired pulse amplitude and frequency were set, flow data were recorded. The anemometer probe was then removed and heat transfer measurements were recorded to eliminate possible flow disturbances. All measurements were continuously synchronized by the electrical pulses generated by the shaft position sensor to allow subsequent association of instantaneous flow and heat transfer readings. Power spectra were also

used to indicate the presence of frequencies related to the pulsations or flow structures. The maximum frequency value (i.e. the Nyquist frequency) that could be detected in the signals at the 4 kHz sampling rate employed in the flow and heat transfer measurements was 2 kHz.

The ensemble-averaging technique was also applied to instantaneous surface heat flux and surface temperature measurements made with the microsensor. The associated waveform amplitudes A_T and A_q were computed as root-mean-squares of the ensemble-averaged data, and were defined as percentages of the mean values. Local convective heat transfer coefficients were determined directly from either ensemble- or time-averaged data of surface heat flux, surface temperature, and jet temperature at the nozzle opening. In these calculations, the net radiative heat flux from the impingement surface was subtracted from the total heat flux to obtain the heat flux due to convection. The net radiative heat flux was formulated by assuming that the impingement surface was a gray, diffuse emitter and reflector, and the surroundings behaved as a black body. Such corrections are common in convective heat transfer studies with radiatively transparent fluids. As defined in practical applications, the time-averaged Nusselt number [equation (9)] was based on nozzle width, time-averaged heat flux, and time-averaged temperature difference:

$$Nu_{avg} = \frac{\overline{q_s}}{\overline{T_s - T_j}} \frac{w}{k(\bar{T}_f)}. \quad (9)$$

Both the steady- and pulsating-flow results of this study pertained closely to a constant surface temperature heating condition ($A_T \approx 0$, as discussed above) with $Pr = 0.7$.

Uncertainties in flow velocities and heat transfer coefficients were estimated according to the method presented by Kline and McClintock [23]. The sequential perturbation technique [20] was used to evaluate sensitivity coefficients which could not be found from explicit relationships. Uncertainties in physical dimensions, thermophysical properties, flow velocities, temperatures, and heat fluxes were considered. The relative error in local Nusselt number ranged from 9.5 to 12%, with the higher uncertainties pertaining to flows of higher jet Reynolds numbers. Uncertainties in measured velocities and Reynolds numbers ranged from 4 to 7%, with the highest uncertainty pertaining to the lowest Reynolds numbers. Repeatability (i.e. run-to-run variations) of all results was within 2%. Measured stagnation region Nusselt numbers for steady jets were within 5% of the theoretical laminar solution [24] for $Re_w = 1000$ and $H/w = 3$, for which $Tu < 1\%$ at the nozzle exit, and the potential core was incident on the surface.

It is important to note that heat transfer processes to pulsating jet flows constitute a complex nonlinear dynamic system [12]. Sinusoidal variations in an incident jet velocity can thereby induce nonsinusoidal responses in instantaneous heat transfer coefficients, even in the absence of incident vortex structures. A theoretical stability map of the hydrodynamic boundary layer response to sinusoidal flow pulsations is shown in Fig. 4. This map was constructed from a detailed semi-analytical nonlinear dynamics model of instantaneous heat transfer to pulsating jet flows [14]. A signed digraph [25] of the linearized system indicated that periodic (stable) responses can be expected in terms of boundary layer momentum and energy transport when the time-averaged eigenvalue stemming from the momentum equation had a negative value [26]. According to Fig. 4, large changes in convective heat transfer coefficients and particularly inter-

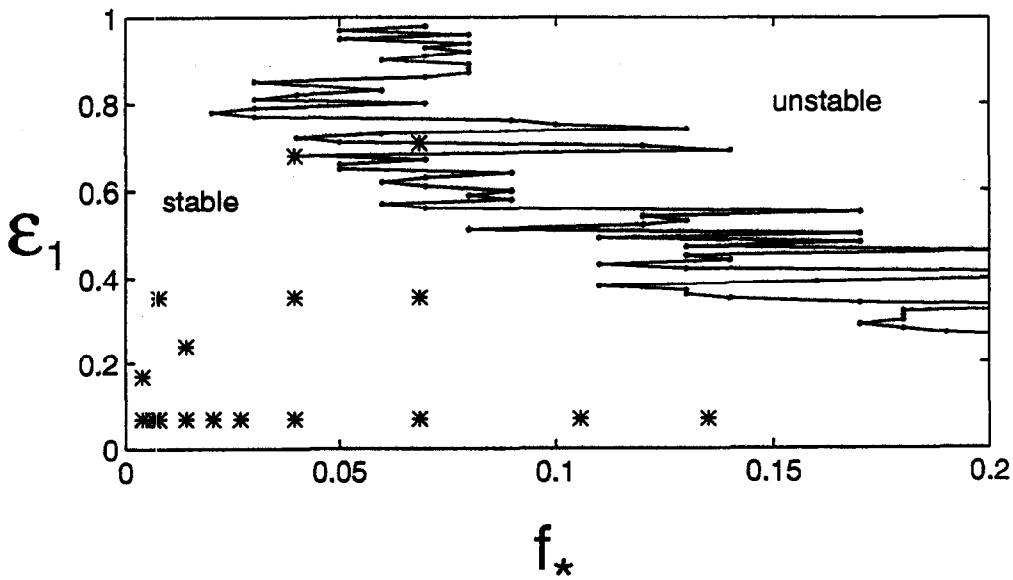

Fig. 4. Theoretical stability map for periodic boundary layer responses to sinusoidal flow pulsations [14].

esting responses may occur within the unstable region where stable boundary layer behavior ceases under combinations of high pulsation frequency and amplitude. Although incident flow structures such as those shown in Fig. 1 may influence boundary layers on the impingement surface, experimental conditions are indicated by asterisks and fall within the stable region of Fig. 4. Complex or chaotic responses are thereby not expected as a result of periodic flow disturbances. Unfortunately, the generation of high-amplitude, high-frequency pulsations is difficult to achieve in fluidic systems. High frequencies can induce significant inertial effects in liquids and compressibility effects in gases, both of which restrict pulse amplitude.

3. RESULTS

As discussed earlier, the heat transfer characteristics of an impinging jet can often be correlated with the characteristics of the corresponding nonimpinging jet [1, 2]. In pulsed flows, the size and formation of coherent structures are influenced by the pulse amplitude and pulse frequency as depicted in Fig. 1. It is therefore instructive to present some representative flow measurements before discussing the heat transfer results. A more complete discussion of the flow measurements has been given by Mladin [27]. Little difference was found in Fig. 5(a) between the time-averaged velocities within the nozzle mid-plane

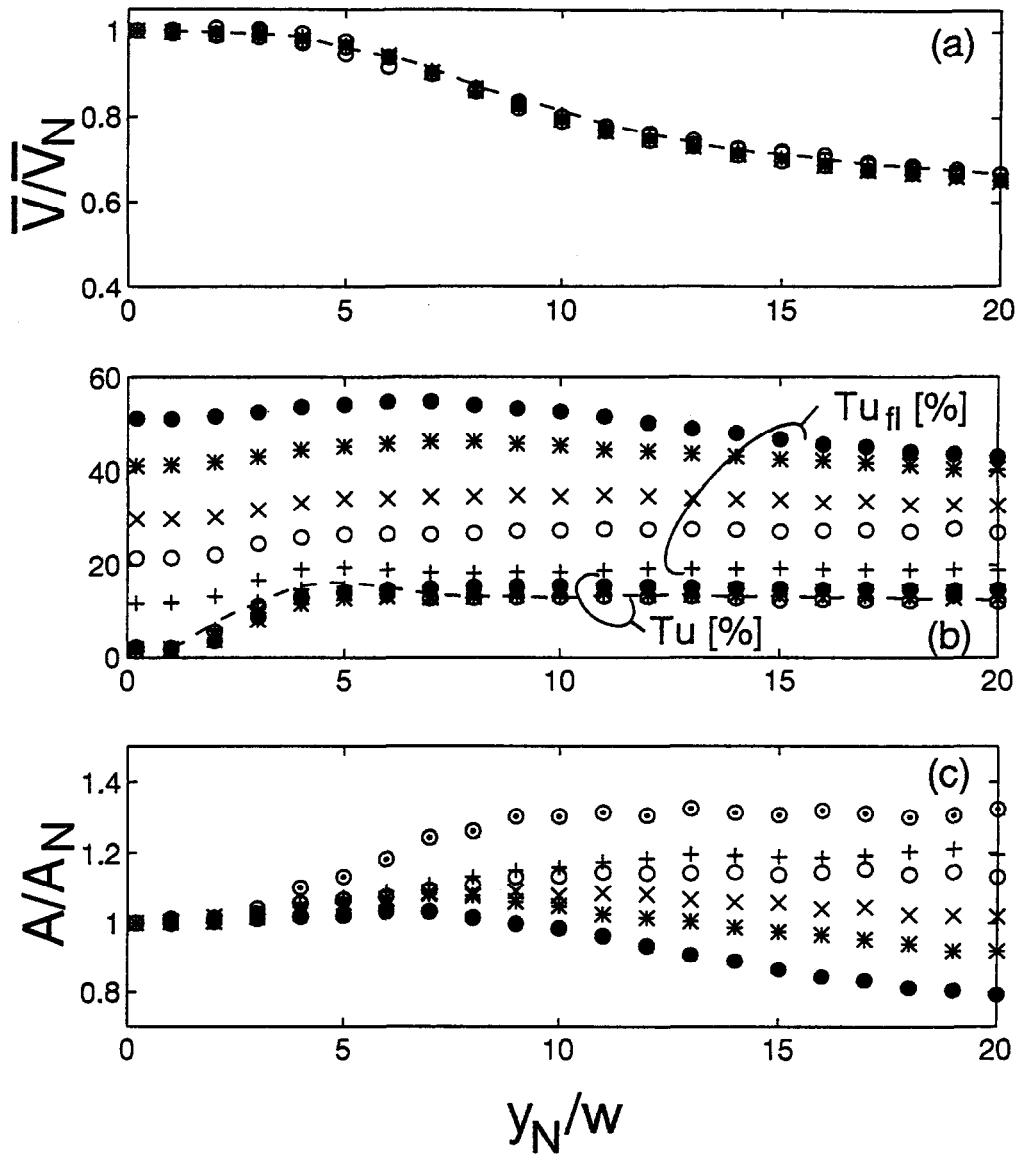

Fig. 5. Influence of pulse amplitude at nozzle exit on centerline velocity (a), turbulence intensity and overall disturbance level (b), and local pulse amplitude (c) for $Re_w = 5500$ and $x = 0$ [---steady jet]: (+) $A_N = 11\%$, $f_{ex} = 39$ Hz, $St_w = 0.011$; (○) $A_N = 21\%$, $f_{ex} = 39$ Hz, $St_w = 0.011$; (x) $A_N = 30\%$, $f_{ex} = 20$ Hz, $St_w = 0.006$; (*) $A_N = 41\%$, $f_{ex} = 20$ Hz, $St_w = 0.006$; (●) $A_N = 51\%$, $f_{ex} = 20$ Hz, $St_w = 0.007$; (⊙) $A_N = 5\%$, $f_{ex} = 82$ Hz, $St_w = 0.024$.

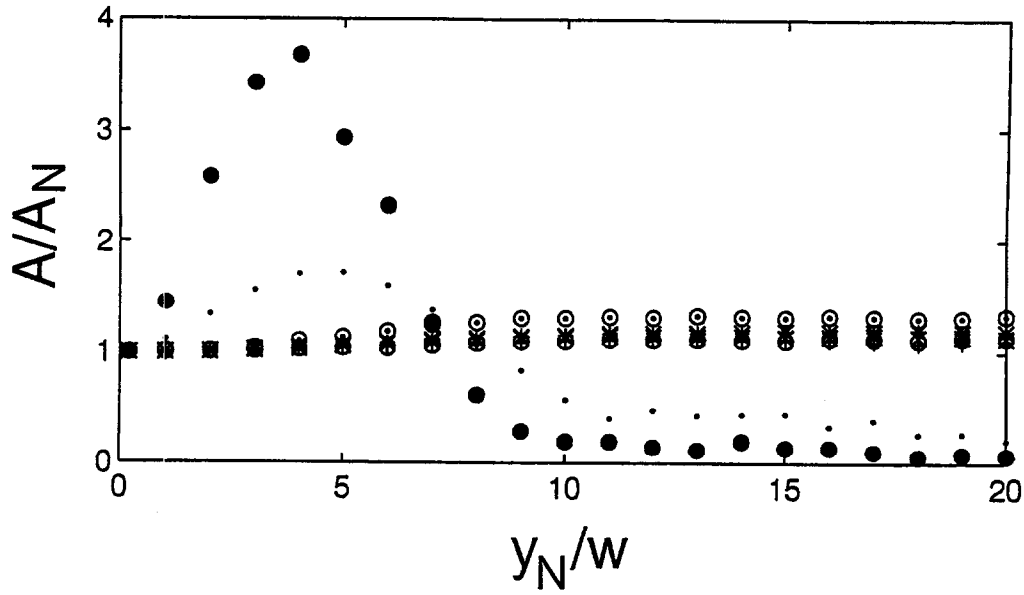

Fig. 6. Streamwise variation of pulse amplitude for $x = 0$: (+) $f_{ex} = 20$ Hz, $St_w = 0.006$, $A_N = 21\%$, $Re_w = 5500$; (○) $f_{ex} = 30$ Hz, $St_w = 0.009$, $A_N = 21\%$, $Re_w = 5500$; (x) $f_{ex} = 40$ Hz, $St_w = 0.011$, $A_N = 21\%$, $Re_w = 5500$; (*) $f_{ex} = 47$ Hz, $St_w = 0.013$, $A_N = 21\%$, $Re_w = 5500$; (⊙) $f_{ex} = 82$ Hz, $St_w = 0.024$, $A_N = 5\%$, $Re_w = 5500$; (•) $f_{ex} = 39$ Hz, $St_w = 0.061$, $A_N = 11\%$, $Re_w = 1000$; (●) $f_{ex} = 82$ Hz, $St_w = 0.130$, $A_N = 5\%$, $Re_w = 1000$.

($x = 0$) for steady and pulsating jets. Similar turbulence levels [Tu in Fig. 5(b)] were also measured even though the presence of the pulse is evident in the overall disturbance levels (Tu_{fl}). Since Tu_{fl} remained above Tu in all cases, pulsations did not completely degrade to turbulence. The local pulse amplitude A at a specific vertical distance from the nozzle opening is related to Tu_{fl} and Tu by equation (5), and is given in Fig. 5(c). Results show that pulses of smaller magnitudes persisted over larger distances, and were more amplified. Such pulse amplifications are consistent with results reported by Hussain and Reynolds [21], and Favre-Marinet and Binder [8]. Near the nozzle opening ($Y_N/w < 4$), values of Tu were lower than those for steady jets. For example, for $y_N/w = 3$, $Tu = 7\%$ for $A_N = 51\%$ in comparison to $Tu = 11\%$ for the steady jet. The lower turbulence intensities taken together with the pulse amplifications may indicate a greater organization in the flow associated with an early formation of vortex structures [6]. For any specific pulse amplitude, pulse amplifications occurred nearer to the nozzle and decayed more abruptly as the Strouhal number was increased. In Fig. 6, pulse amplitude increased significantly relative to the amplitude at the nozzle exit only for the highest Strouhal numbers in combination with the lowest pulse amplitude of 5%. Jet centerline velocities, turbulence intensities, and total disturbance levels for the high Strouhal number cases of Fig. 6 are given in Fig. 7. Early vortex generation led to a slight decrease in the jet velocity and slightly reduced turbulence levels for $y_N/w < 5$. The pulse amplification of Fig. 6 and increasing turbulence intensities increased overall disturbance levels within this same region. Far from the nozzle exit, overall disturbance levels merged with turbulence intensities as the pulse abated. Degeneration of the pulsed flow led to turbulence intensities higher than those of the corresponding steady jet. From a practical standpoint, it is apparent that pulses of high Strouhal number degenerated more rapidly, so that smaller nozzle-to-plate separation distances are necessary under such conditions for pulsations and induced flow structures to persist and directly affect heat transfer.

The pulse frequency and associated Strouhal number significantly influenced the formation and interaction of the coherent flow structures in the non-impinging pulsed jets. In power spectra of the velocity V', the initial flow structures such as those of Fig. 1 were characterized by the pulsation frequency f_{ex}. Vortex pairing (i.e. the merging of two similar vortices to yield a larger vortex [5]) was indicated by the emergence of a subharmonic frequency of $0.5f_{ex}$. The streamwise distance between two successive flow structures was indicated by two successive in-phase periodic velocities. The corresponding spatial wavelength λ remained constant over the downstream distance where the pulse was still significant, as indicated by the dominance of f_{ex} in the power spectra of V'. The spatial wavelength λ scaled according to $[w(2St_w)^{-1}]$. After the pulse degraded, the dominant frequency in the power spectra decreased with increasing distance from the nozzle.

The variation of Nusselt number at the nozzle midplane ($x = 0$) with nozzle-to-plate separation distance is shown for specific Strouhal numbers in Fig. 8. Results pertaining to $Re_w = 1000$ and $St_w = 0.054$ are compared to those of the steady jet in Fig. 8(a). For

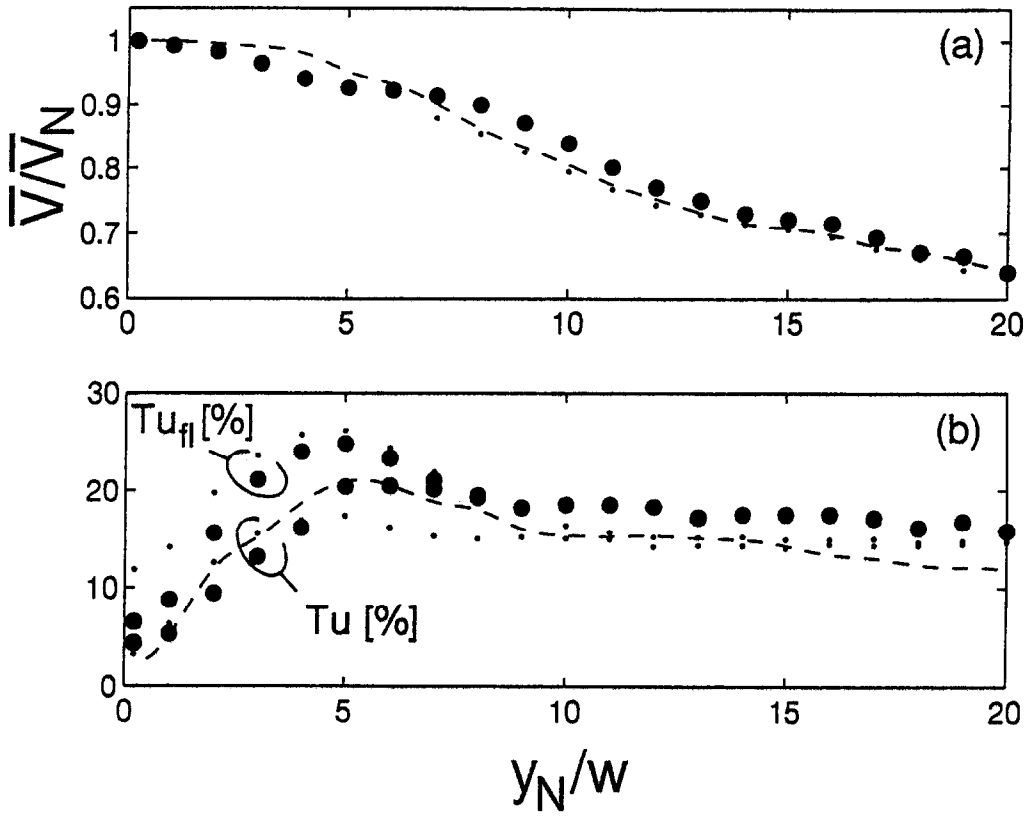

Fig. 7. Influence of pulse frequency on mean centerline velocity (a) and turbulence intensity and overall disturbance level (b) for $Re_w = 1000$ and $x = 0$ [– – –steady jet: (•) $f_{ex} = 39$ Hz, $St_w = 0.061$, $A_N = 11\%$; (●) $f_{ex} = 82$ Hz, $St_w = 0.130$, $A_N = 5\%$].

$A_N = 5\%$, little effect on Nusselt number was discerned. Differences of less than 2% were comparable to the experimental repeatability. For $A_N = 25\%$, Nu_{wS} was enhanced by about 8% at $H/w = 5$. For the highest amplitude, $A_N = 50\%$, the Nusselt number was enhanced by 12% at $H/w = 3$. As the pulse amplitude was increased, the largest enhancement was greater and occurred at smaller separation distances. This was attributed to the formation of larger flow structures nearer to the nozzle, based on flow visualization performed by Farrington and Claunch [6] in similar planar air jet flows. Enhancements due to improved mixing caused by early vortex formation decreased sharply for $H/w > 6$, and decreased at a faster rate for higher pulse magnitudes. As shown in Fig. 7 for a similar Strouhal number, flow organization and the associated pulse amplification yielded reduced turbulence intensities over a distance about 10 nozzle widths from the nozzle exit. Enhancements decreased as a consequence and time-averaged Nusselt numbers for the pulsed jets for $6.5 < H/w < 10$ in Fig. 8(a) eventually became lower than those for the steady jet.

Results for a higher Reynolds number and a lower Strouhal number are shown in Fig. 8(b). Although the pulsation frequency is identical to the one for Fig. 8(a), the Strouhal number was lower due to a higher jet velocity. Departures of Nusselt numbers from corresponding steady-jet values ranged from −8 to +5%. The diminished Nusselt numbers at small separation distances may be attributed to nonlinear dynamic effects in momentum and energy transport within the boundary layers. Reductions are consistent with the theoretical nonlinear dynamic model predictions [14] for a similar pulsation frequency, and arise since sinusoidal flow variations can induce nonsinusoidal responses due to nonlinearities in transport processes. In effect, thermal boundary layer thicknesses become larger on average as a result of pulsations. Van der Hegge Zijen [28] also reported that the heat transfer from a wire vibrating in the direction of an uniform air flow was lower than the heat transfer from a stationary wire, and the corresponding Nusselt number decreased with increasing vibration amplitude. The nonlinear dynamic effect reflects that the disturbances associated with flow pulsation do not allow momentum and energy transfer to equilibrate within the boundary layers. Slightly increased turbulence intensity levels in the pulsed jets, as indicated by flow-field measurements in nonimpinging jets of the same Reynolds number, led to small heat transfer enhancements for $H/w > 6$. For $Re_w = 11\,000$ and $St_w = 0.003$, stagnation line Nusselt numbers in Fig. 8(c) remained close to the steady-jet values for $H/w < 6$. Over such distances, the free-stream turbulence in the corresponding nonimpinging

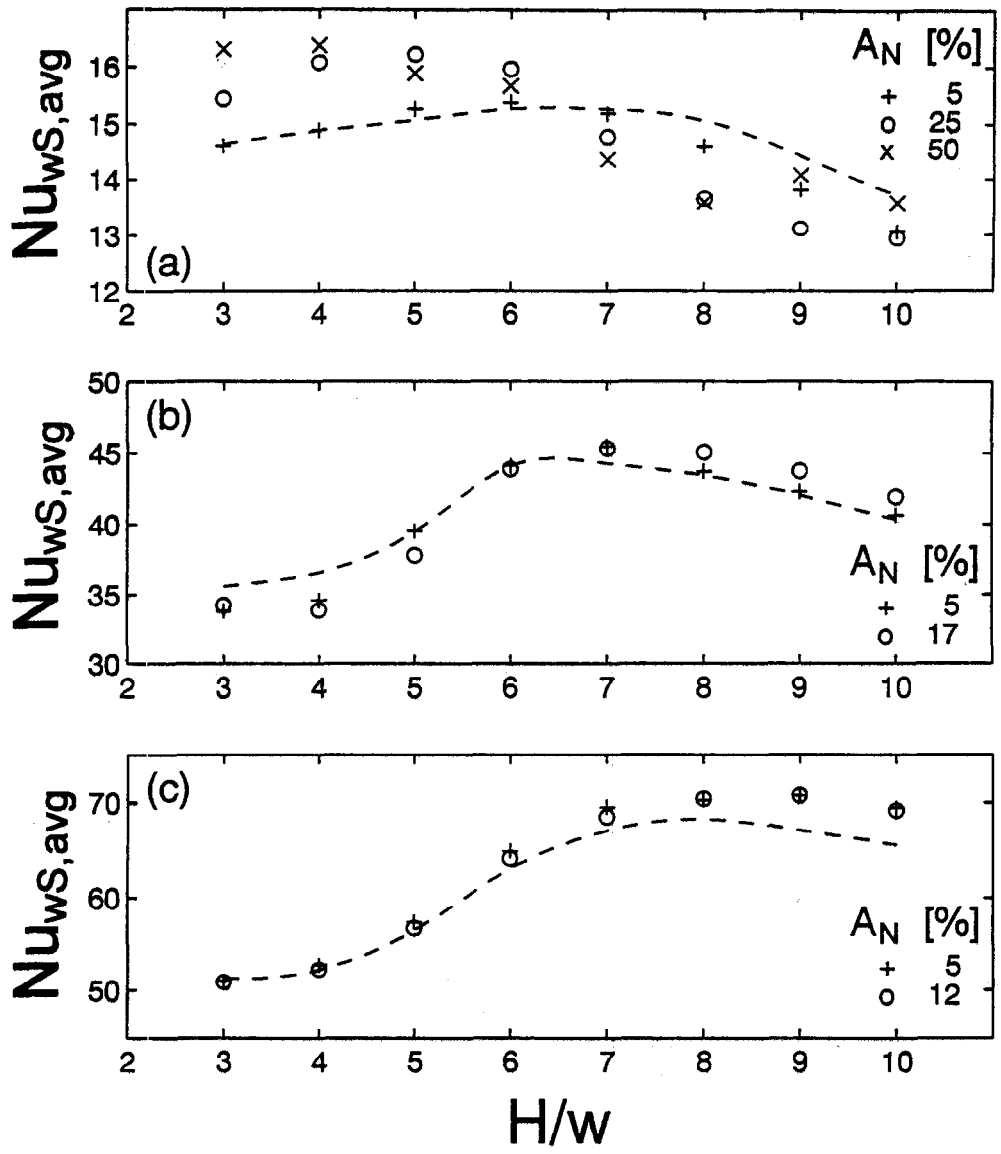

Fig. 8. Influence of pulse amplitude on time-averaged Nusselt number in the nozzle mid-plane: (a) $Re_w = 1000, f_{ex} = 41$ Hz, $St_w = 0.054$; (b) $Re_w = 5500, f_{ex} = 41$ Hz, $St_w = 0.011$; (c) $Re_w = 11\,000, f_{ex} = 23$ Hz, $St_w = 0.003$ [---steady jet].

pulsed jet was about the same as for the steady jet, and the pulse had an essentially constant amplitude. This result suggested that the organized motion from the low-amplitude/low-Strouhal-number pulse did not interact with the mean flow, nor did it degrade into turbulent motion. For $H/w > 6$, the Nusselt number was enhanced by as much as 6%. This increase was consistent with a measured increased turbulence associated with the decay of large flow structures in the far flow field, as in Fig. 8(b).

Nusselt number distributions for conditions identical to those of Fig. 8 are shown in Fig. 9. Increased Nusselt numbers occurred for $A_N > 5\%$ in Fig. 9(a) with $Re_w = 1000$. Increases were most pronounced in the wall jet region ($x/w > 2$), where the favorable pressure gradient in the stagnation region subsided, and flow instabilities in the boundary layer can grow more readily. Nusselt numbers for $A_N = 50\%$ increased above the steady-jet case by 35% at $x/w = 6$, and by 80% at $x/w = 10$. An earlier transition to turbulence is also suggested in Fig. 9(b) at the higher pulse amplitudes. Beyond two nozzle widths from the stagnation line, the local Nusselt number was about 25% above the steady-jet case. Since measurements in Fig. 9(b) pertained to $H/w = 5$, it is interesting to note that flow-field measurements in the corresponding nonimpinging pulsed jet at four nozzle widths downstream from the nozzle opening indicated an increased turbulence intensity level and a modest pulse amplification. In the presence of the impingement plate, larger fluctuations in the instantaneous surface heat fluxes were recorded, suggesting that a higher incident

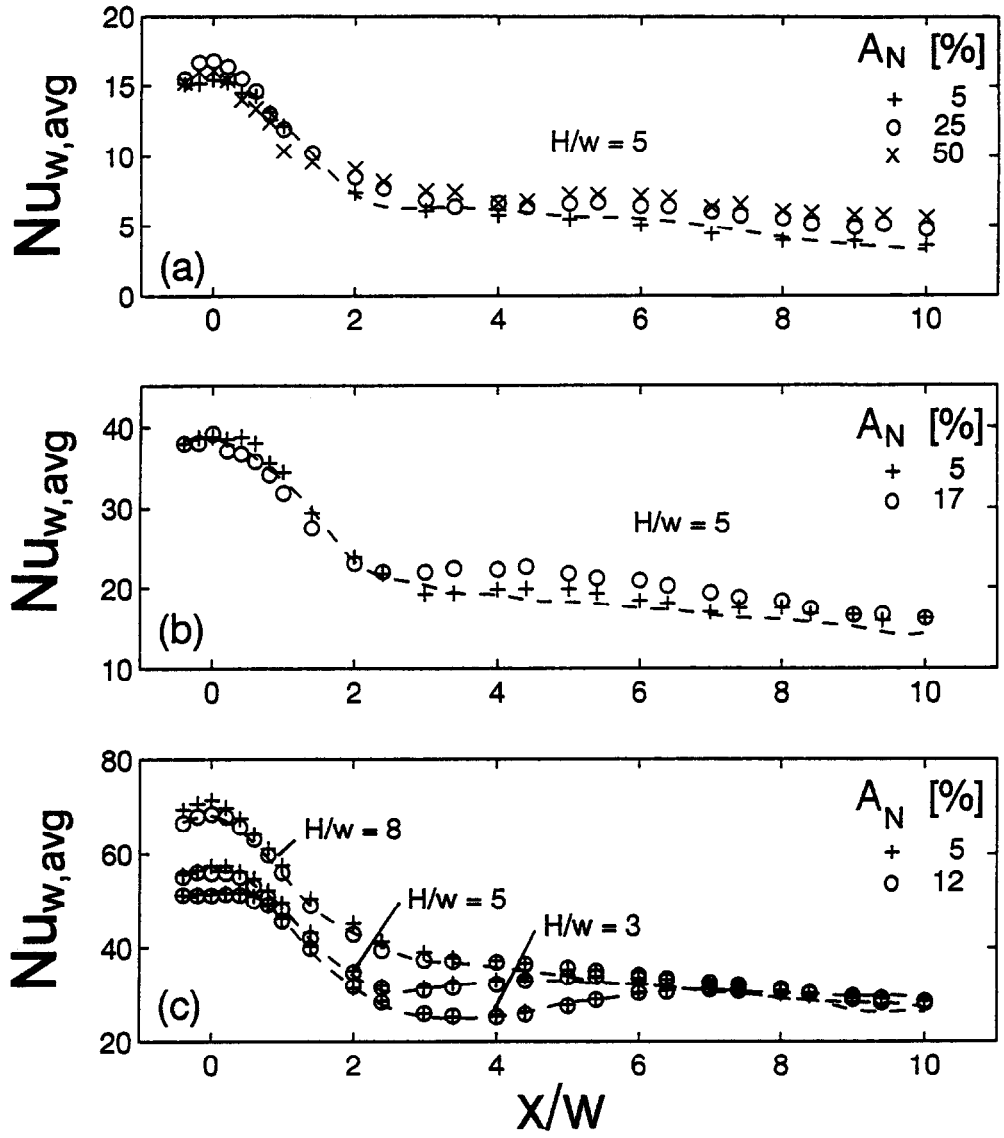

Fig. 9. Influence of pulse amplitude on time-averaged Nusselt number distribution: (a) $Re_w = 1000, f_{ex} = 41$ Hz, $St_w = 0.054$; (b) $Re_w = 5500$, $f_{ex} = 41$ Hz, $St_w = 0.011$; (c) $Re_w = 11\,000$, $f_{ex} = 23$ Hz, $St_w = 0.003$ [– – –steady jet].

free-stream turbulence was carried near the surface. The heat transfer enhancements may therefore be attributed to increased free stream turbulence intensities stemming from the interaction of flow structures with the surface. This enhancement mechanism is supported by the observed formation of small eddies just above an impingement surface and adjacent to an impinging jet as a result of incident large-scale vortices [4]. At the highest Reynolds number ($Re_w = 11\,000$) and correspondingly lowest Strouhal number of Fig. 9(c), no significant changes in heat transfer characteristics were evident.

The variation of Nusselt number in the nozzle mid-plane ($x = 0$) with nozzle-to plate separation distance is shown for various pulsation frequencies in Fig. 10. For these results, $A_N = 5\%$ was a value that could be experimentally achieved over the entire range of pulse frequencies. In Fig. 10(a) with $Re_w = 1000$, $0.03 < St_w < 0.106$, and $H/w < 6$, the Nusselt number increased by up to 5% with increasing f_{ex} compared to the steady-jet case. In contrast, at higher H/w, the Nusselt number decreased by as much as 8%. For $Re_w = 5500$ and $0.006 < St_w < 0.021$, Nusselt numbers in Fig. 10(b) were as much as 10% below steady-jet values at $H/w = 3$. However, enhancement of about 6% occurred for $H/w = 10$. For $Re_w = 11\,000$ in Fig. 10(c), a maximum increase of 5% occurred at $H/w = 10$, with no measurable differences at smaller separation distances. Thus, flow pulsations most greatly influenced the Nusselt number in the nozzle mid-plane at the highest Strouhal numbers which correspond to the lowest jet Reynolds number. As demonstrated in Fig. 6, high Strouhal number pulses of small amplitude were highly amplified near the

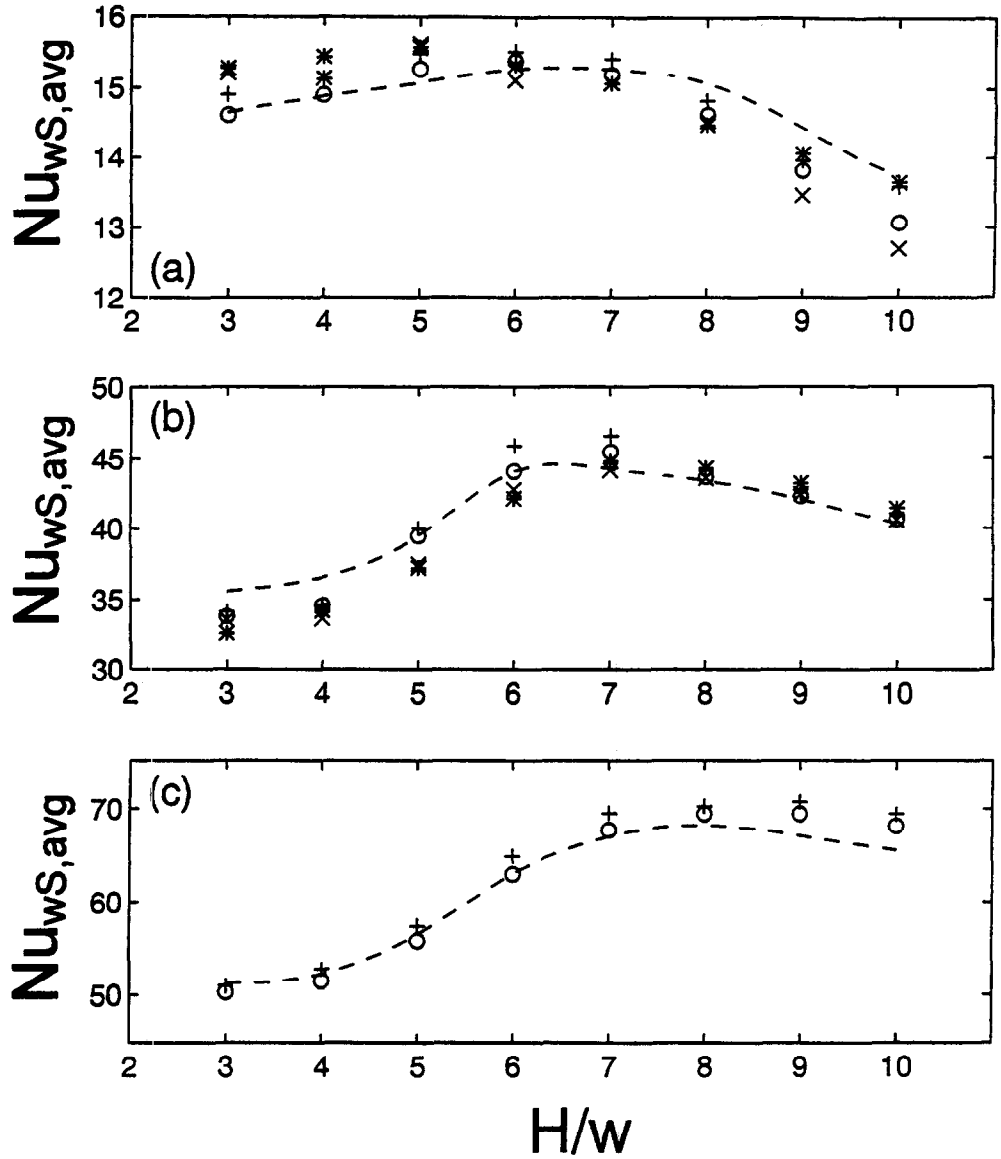

Fig. 10. Influence of pulse frequency on time-averaged Nusselt number in the nozzle mid-plane: (a) $Re_w = 1000$, $A_N = 5\%$, $0.03 < St_w < 0.106$; (b) $Re_w = 5500$, $A_N = 5\%$, $0.006 < St_w < 0.021$; (c) $Re_w = 11\,000$, $A_N = 5\%$, $0.003 < St_w < 0.005$ [---steady jet, (+) $f_{ex} = 23$ Hz, (○) $f_{ex} = 41$ Hz, (×) $f_{ex} = 62$ Hz, (*) $f_{ex} = 80$ Hz].

nozzle. Therefore, opportunities for enhancements are suggested for such conditions when the nozzle-to-plate distances are small. Enhancements are attributed to surface renewal effects [7] related to incident flow structures (Fig. 1) in light of the pulse amplifications, and since turbulence levels were depressed near the nozzle opening as shown in Figs. 5 and 7.

At large separation distances (e.g. $H/w > 6$), accelerated degeneration of flow structures in high Strouhal number flows yielded both decreases or increases in Nusselt numbers, depending on ensuing turbulence levels and the extent of vortex break down. Although not shown, Nusselt numbers away from the nozzle mid-plane which corresponded to Fig. 10 increased by about 25% for $x/w > 3$ only for the intermediate Reynolds number ($Re_w = 5500$) and Strouhal number range ($0.006 < St_w < 0.021$) [27]. No measurable difference occurred between local Nusselt numbers for the steady and pulsating jets with $Re_w = 1000$ or $Re_w = 11\,000$. For $Re_w = 1000$, the pulse amplitude ($A_N = 5\%$) was too small to promote an earlier transition to turbulence in the wall jet region. For $Re_w = 11\,000$, turbulence levels in the pulsating jet remained nearly identical to those of the unforced jet. These results indicate that both pulse amplitude and pulse frequency must be sufficiently high to influence heat transfer conditions at the stagnation line, as well as in the wall jet region. Although more experimental study is needed to confirm a relationship, the ensemble-averaged Navier–Stokes equations for a sinu-

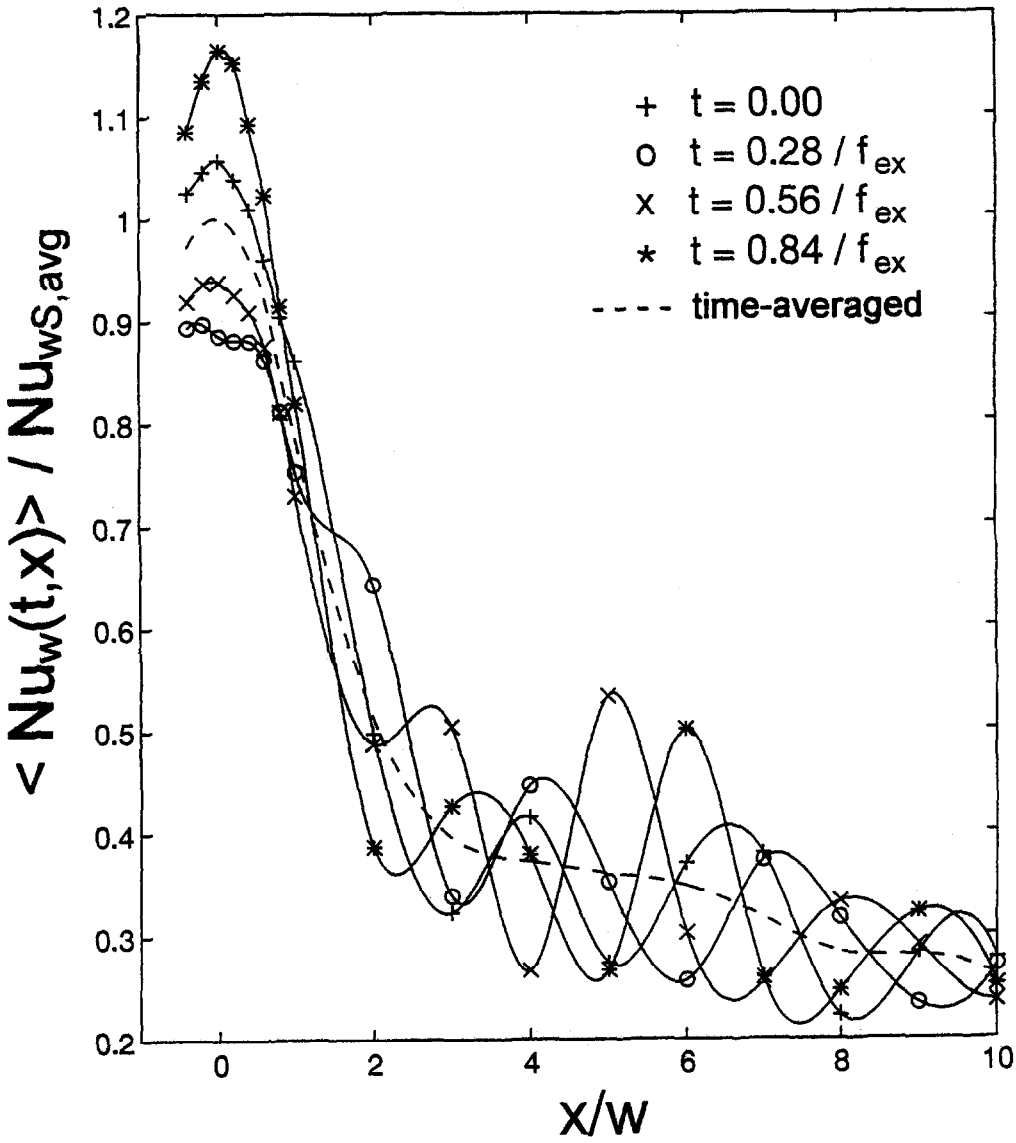

Fig. 11. Instantaneous Nusselt number distributions for $Re_w = 1000$, $f_{ex} = 80$ Hz ($St_w = 0.106$), $A_N = 5\%$, and $H/w = 5$.

soidally varying incident flow suggest that the product $St_w A_N$ is pertinent to the flow field [8], and may therefore also be an effective correlating parameter for heat transfer.

A representative instantaneous convective heat transfer distribution is presented in Fig. 11 in terms of ensemble-averaged local Nusselt numbers [equation (2)]. Values are referenced to the time-averaged Nusselt number in the nozzle mid-plane to emphasize the relative magnitude of the instantaneous fluctuations. The ensemble-averaging technique removed the random fluctuations due to turbulence from the instantaneous heat transfer data, but preserved the fluctuations from the periodic, organized fluid motion. By doing so, smooth distributions can be constructed with data from the single microsensor of Fig. 3 and synchronized with the flow pulsations. For the sake of clarity, instantaneous distributions are given at four instants of time equally separated over one pulsation period ($1/f_{ex}$). Fluctuations in $\langle Nu_w \rangle$ were highest in the nozzle mid-plane and at about five nozzle widths downstream. In the nozzle midplane, variations in flow velocity, nozzle exit velocity, and $\langle Nu_w \rangle$ shared the same principal frequency, but phase differences were detected owing to the advection of flow structures to the surface. Interestingly, very small fluctuations occurred in instantaneous Nusselt numbers for $x/w \approx 1$, where fluid acceleration was significant in response to the favorable pressure gradient, and turbulence abatement occurred. Consequently, measurable enhancements were not obtained in Figs. 9 and 11 within this narrow region even when significant enhancements occurred nearer to the nozzle mid-plane and downstream. The corresponding power spectra

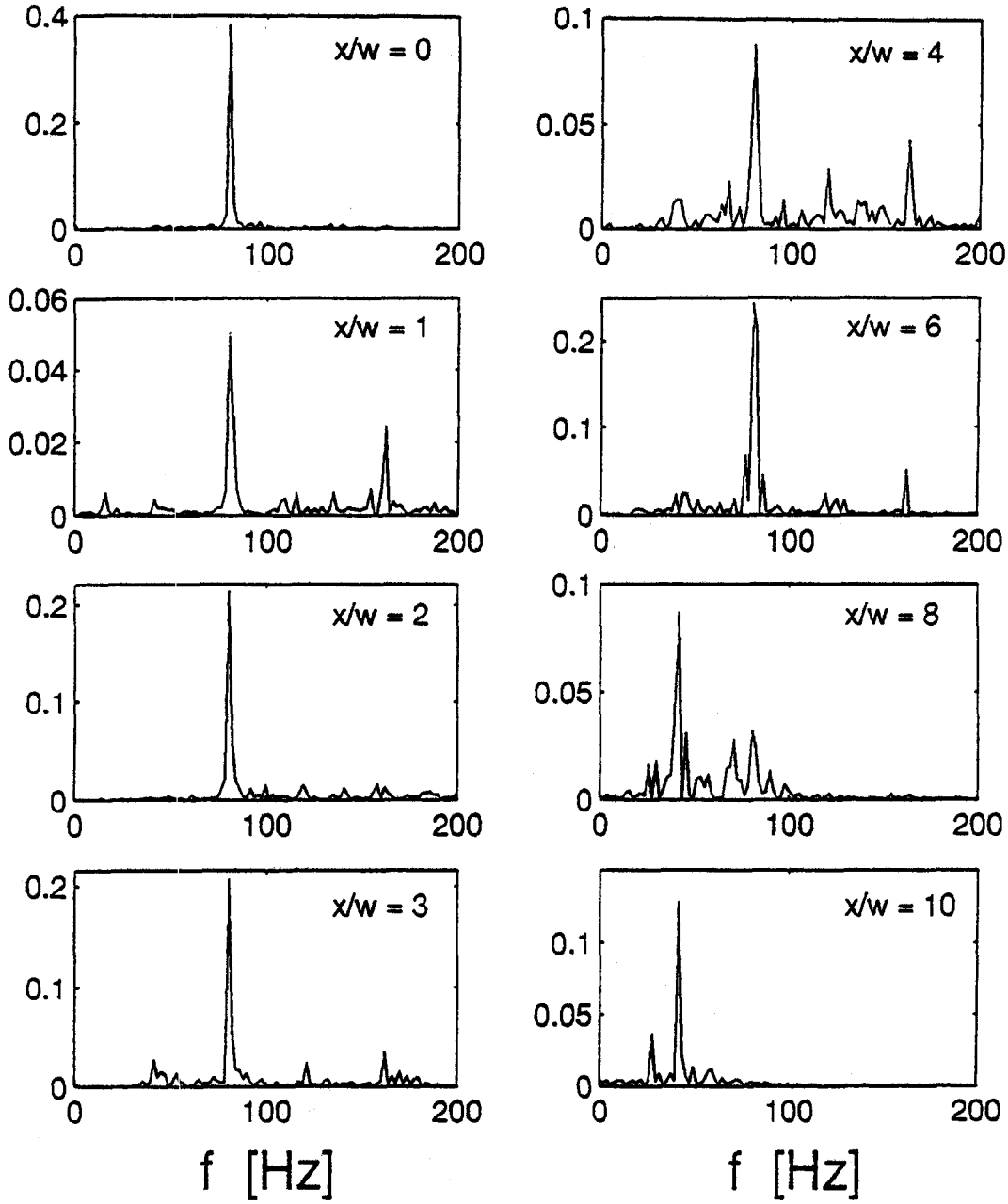

Fig. 12. Frequency spectra of local heat fluxes for the conditions of Fig. 11.

for the local heat flux are shown in Fig. 12. In the nozzle mid-plane ($x/w = 0$), a single spike at 80 Hz corresponded to the pulse frequency. Magnitudes of disturbances were smallest for $x/w \approx 1$, where the smallest differences arose in Fig. 11. Spatial wavelengths (λ_x) for periodic spatial fluctuations in instantaneous local Nusselt numbers correlated approximately with the dominant frequencies in the incident flow according to $\lambda_x \sim w/(4St_w)$. A correspondence between the incident flow structures and the local heat transfer was thereby indicated. The frequency content broadened increasingly at distances further downstream. This broadening occurred preferentially at frequencies above the pulse frequency for $x/w < 4$, and may have been associated with the breakdown of incident vortices and an ensuing turbulence. Further from the nozzle mid-plane, a signal with a frequency about half the pulse frequency became dominant, and was accompanied by other frequencies lower than f_{ex}. Such lower frequencies may be related to the intrusion into the boundary layer of larger vortices stemming from vortex pairing events [5] above the impingement plate. Alternately, they may reflect stretching of flow structures as a result of the preceding favorable pressure gradient. Uncertainty in the prevailing cause points to a need for additional flow visualization of impinging,

pulsating flows. The abatement of the high-frequency content for $x/w > 8$ was accompanied by decreased fluctuations in instantaneous Nusselt numbers in Fig. 11.

4. CONCLUSIONS

Changes in flow structures, turbulence levels, and nonlinear dynamic effects in impinging submerged jets subjected to flow pulsations led to alterations in convective heat transfer. Enhancements or reductions along the impingement surface depended strongly on parametric conditions. Pulsations have been shown in prior studies to promote a more regular formation of vortices nearer to the nozzle opening in comparison to steady flows in both circular and planar jet flows. Anemometry measurements of this study indicated that this organized fluid motion depressed turbulence levels in the vicinity of the nozzle opening, and resulted in pulse amplifications. Peak alterations at the stagnation line corresponded to nozzle-to-plate separation distances where the pulse in the corresponding nonimpinging jet was most amplified. Heat transfer enhancements up to 12% near the nozzle mid-plane due to surface renewal effects, and up to 80% at distances downstream due to increased turbulence levels, were measured where both the pulse amplitude and Strouhal number were highest. It is conjectured that enhancements can be obtained under combinations of pulse amplitude and frequency which lie in or near the unstable region of Fig. 4. Flow pulsations alternately induced measurable reductions (i.e. $>2\%$) in time-averaged Nusselt numbers in the stagnation region when the potential core was incident on the surface. For this situation, nonlinear dynamic responses to flow pulsations in momentum and energy transport induce thicker boundary layers on average and diminish heat transfer. Such responses were in good agreement with a nonlinear dynamics model developed separately for boundary layer flows, and conditions for the reductions have been specified [14]. Pulses of small amplitude and low frequency induced a quasi-steady behavior at small separation distances, with no discernible effect on the time-averaged Nusselt number in the vicinity of the nozzle mid-plane. However, at larger separation distances, increased turbulence associated with the decay of the flow pulse enhanced the time-averaged Nusselt number away from the nozzle mid-plane by up to 20%. Spatial wavelengths for fluctuations in instantaneous local Nusselt numbers correlated with frequency spectra of the incident flow, and suggested a correspondence to incident flow structures. Very small fluctuations occurred in instantaneous Nusselt numbers for $x/w \approx 1$, where fluid acceleration in response to the favorable pressure gradient was significant. Consequently, measurable enhancements were not obtained within this narrow region even when significant enhancements occurred nearer to the nozzle mid-plane and at more distant points downstream. Essentially instantaneous local heat transfer measurements with a heat flux microsensor were useful in associating flow-related phenomena with enhancement mechanisms.

Acknowledgements—Support for this work was provided by the National Science Foundation of the United States of America under Grant no. CMS-9253640 in conjunction with a Presidential Faculty Fellow Award to D. A. Zumbrunnen.

REFERENCES

1. Donaldson, C. D. and Snedeker, R. S., A study of free jet impingement. Part 1. Mean properties of free and impinging jets. *Journal of Fluid Mechanics*, 1971, **45**, 281–319.
2. Donaldson, C. D., Snedeker, R. S. and Margolis, D. P., A study of free jet impingement. Part 2. Free jet turbulent structure and impingement heat transfer. *Journal of Fluid Mechanics*, 1971, **45**, 477–512.
3. Ho, C. M. and Huang, L. S., Subharmonics and vortex merging in mixing layers. *Journal of Fluid Mechanics*, 1982, **119**, 443–473.
4. Popiel, C. O. and Trass, O., Visualization of a free and impinging round jet. *Experimental Thermal and Fluid Science*, 1991, **4**, 253–264.
5. Rockwell, D. O. and Niccolls, W. O., Natural breakdown of planar jets. *Journal of Basic Engineering*, 1972, **94**, 720–728.
6. Farrington, R. B. and Claunch, S. D., Infrared imaging of large-amplitude, low-frequency disturbances on a planar jet. *AIAA Journal*, 1994, **32**, 317–323.
7. Kataoka, K., Suguro, M., Degawa, H., Maruo, K. and Mihata, I., The effect of surface renewal due to large-scale eddies on jet impingement heat transfer. *International Journal of Heat and Mass Transfer*, 1987, **30**, 559–567.
8. Favre-Marinet, M. and Binder, G., Structure des jets pulsants. *Journal de Mechanique*, 1979, **18**, 355–394.
9. Nevins, R. G. and Ball, H. D., Heat transfer between a flat plate and a pulsating impinging jet. *Proceedings of the National Heat Transfer Conference, Boulder, CO*, Vol. 60. ASME, New York, 1961, pp. 510–516.
10. Zumbrunnen, D. A. and Aziz, M., Convective heat transfer enhancement due to intermittency in an impinging jet. *Journal of Heat Transfer*, 1993, **115**, 91–98.
11. Zumbrunnen, D. A., Transient convective heat transfer in planar stagnation flows with time-varying surface heat flux and temperature. *Journal of Heat Transfer*, 1992, **114**, 85–93.
12. Mladin, E. C. and Zumbrunnen, D. A., Nonlinear dynamics of hydrodynamic and thermal boundary layers in laminar stagnation flows. *Journal of Thermophysics and Heat Transfer*, 1994, **8**, 514–523.
13. Sheriff, H. S. and Zumbrunnen, D. A., Effect of flow pulsations on the cooling effectiveness of an impinging planar water jet. *Journal of Heat Transfer*, 1994, **116**, 886–895.
14. Mladin, E. C. and Zumbrunnen, D. A., Dependence of heat transfer to a pulsating stagnation flow on pulse characteristics. *Journal of Thermophysics and Heat Transfer*, 1995, **9**, 181–192.
15. Azevedo, L. F. A., Webb, B. W. and Queiroz, M., Pulsed air jet impingement heat transfer. *Experimental Thermal and Fluid Science*, 1994, **8**, 206–213.
16. Sheriff, H. S. and Zumbrunnen, D. A., Local and instantaneous heat transfer characteristics of arrays of pulsating jets. *Proceedings of the ASME Heat Transfer Division*, **HTD-333**, 1996, 101–112.
17. Martin, H., Heat and mass transfer between impinging gas jets and solid surfaces. In *Advances in Heat Transfer*, Vol. 13, Academic Press, New York, 1977, pp. 1–60.

18. Hager, J. M., Simmons, S., Smith, D., Onishi, S., Langley, L. W. and Diller, T. E., Experimental performance of a heat flux microsensor. *Journal of Engineering for Gas Turbines and Power*, 1991, **113**, 246–250.
19. Holmberg, D. G. and Diller, T. E., High-frequency heat flux sensor calibration and modeling. *Journal of Fluids Engineering*, 1995, **117**, 659–664.
20. Moffat, R. J., Describing the uncertainties in experimental results. *Experimental Thermal and Fluid Science*, 1988, **1**, 3–17.
21. Hussain, A. K. M. F. and Reynolds, W. C., The mechanics of an organized wave in turbulent shear flow. *Journal of Fluid Mechanics*, 1970, **41**, 241–258.
22. Evans, R. L., Turbulence and unsteadiness measurements downstream of a moving blade. *Journal of Engineering for Power*, 1975, **97**, 131–139.
23. Kline, S. J. and McClintock, F. A., Describing uncertainties in single sample experiments. *Mechanical Engineering*, 1953, **75**, 3–8.
24. Evans, H. L., Mass transfer through laminar boundary layers. 7. Further similar solutions to the B-equation for the case $B = 0$. *International Journal of Heat and Mass Transfer*, 1962, **5**, 35–37.
25. Jeffries, C. D., *Mathematical Modeling in Ecology: a Workbook for Students*, Birkhauser, Boston, MA, 1991, pp. 36–68.
26. Hale, J. K. and Koçak, H., *Dynamics and Bifurcations*. Springer-Verlag, New York, 1991.
27. Mladin, E. C., Instantaneous convective heat transfer to pulsating submerged jets. PhD thesis, Clemson University, Clemson, SC, 1995.
28. Van der Hegge Zijen, B. G., Heat transfer from horizontal cylinders to a turbulent air flow. *Applied Scientific Research*, 1958, **7(A)**, 205–223.